

Crystal-chemical origins of the ultrahigh conductivity of metallic delafossites

Received: 11 September 2023

Accepted: 15 January 2024

Published online: 15 February 2024

 Check for updates

Yi Zhang ¹, Fred Tutt ¹, Guy N. Evans², Prachi Sharma ^{1,3}, Greg Haugstad⁴, Ben Kaiser¹, Justin Ramberger ¹, Samuel Bayliff ³, Yu Tao ¹, Mike Manno ¹, Javier Garcia-Barriocanal⁴, Vipul Chaturvedi ¹, Rafael M. Fernandes ³, Turan Birol ¹, William E. Seyfried Jr.² & Chris Leighton ¹ ✉

Despite their highly anisotropic complex-oxidic nature, certain delafossite compounds (*e.g.*, PdCoO₂, PtCoO₂) are the most conductive oxides known, for reasons that remain poorly understood. Their room-temperature conductivity can exceed that of Au, while their low-temperature electronic mean-free-paths reach an astonishing 20 μm. It is widely accepted that these materials must be ultrapure to achieve this, although the methods for their growth (which produce only small crystals) are not typically capable of such. Here, we report a different approach to PdCoO₂ crystal growth, using chemical vapor transport methods to achieve order-of-magnitude gains in size, the highest structural qualities yet reported, and record residual resistivity ratios (> 440). Nevertheless, detailed mass spectrometry measurements on these materials reveal that they are not ultrapure in a general sense, typically harboring 100s-of-parts-per-million impurity levels. Through quantitative crystal-chemical analyses, we resolve this apparent dichotomy, showing that the vast majority of impurities are forced to reside in the Co-O octahedral layers, leaving the conductive Pd sheets highly pure (~1 ppm impurity concentrations). These purities are shown to be in quantitative agreement with measured residual resistivities. We thus conclude that a sublattice purification mechanism is essential to the ultrahigh low-temperature conductivity and mean-free-path of metallic delafossites.

Complex oxide materials have proven to be fertile ground for the discovery of new physical phenomena and the advancement of technologically important device function, the ABO₃ perovskites being a prime example^{1–4}. Many related classes of complex oxides offer similarly substantial potential but remain less extensively studied. ABO₂ delafossites are one example, where two-dimensional triangular sheets of typically monovalent A ions are separated by layers of edge-shared BO₆ octahedra^{5–10}. Most delafossite compounds are insulating or semiconducting, such as the CuFeO₂ studied for frustrated magnetism^{11,12} and the CuAlO₂ considered for transparent conductive

oxide applications¹³. It has been known since 1971, however^{5–8}, that some delafossites exhibit metallic character, exemplified by PdCoO₂ and PtCoO₂. These metallic delafossites received little attention until the relatively recent discovery that, in bulk-single-crystal form, they are the most conductive oxides known^{5,10}. While their *c*-axis resistivities (ρ_c) are more than 100 times higher^{5,8,9,14–16}, the room-temperature *a*-*b*-plane resistivities (ρ_{ab}) of PdCoO₂ and PtCoO₂ are only 3.1 and 1.8 μΩcm, respectively¹⁷, comparable to or lower than Au⁵. Their low-temperature (*T*) residual ρ_{ab} values fall as low as 8.1 nΩcm¹⁷, implying residual resistivity ratios (RRRs) up to 376¹⁷ and low-*T* mean-free paths

¹Department of Chemical Engineering and Materials Science, University of Minnesota, Minneapolis, MN 55455, USA. ²Department of Earth and Environmental Sciences, University of Minnesota, Minneapolis, MN 55455, USA. ³School of Physics and Astronomy, University of Minnesota, Minneapolis, MN 55455, USA.

⁴Characterization Facility, University of Minnesota, Minneapolis, MN 55455, USA. ✉ e-mail: leighton@umn.edu

of $\sim 20 \mu\text{m}^{5,15}$. These are astonishing values, particularly in complex oxides, in such highly anisotropic structures, and given the relatively little materials development performed.

The electronic structure of metallic delafossites is similarly noteworthy. Taking PdCoO_2 as an example, the established $R\bar{3}m$ structure of the $3R$ polymorph^{5–7,9,10,18} results in a strikingly simple electronic structure where a single Pd d band crosses the Fermi level, with only modest contributions from Co, and negligible O character^{5,9,10,18–21}. The Pd d band is highly dispersive^{5,9,10,18–22}, potentially assisted by a contribution from Pd s states^{23,24}. The triangular Pd¹⁺ planes thus generate a Fermi surface closely approximating a hexagonal-cross-section cylinder filling half the hexagonal Brillouin zone in the a^*b^* reciprocal-space plane^{5,15,18–21,25,26}. The remarkable simplicity of this electronic structure is underscored by electron effective masses of only 1–1.7 m_e ^{5,15,18,27}. The edge-shared CoO_6 octahedra also have short Co–O bond lengths and large crystal field splitting, stabilizing low-spin ($S=0$) Co^{3+18} . PdCoO_2 is thus a model metallic delafossite, which can be thought of as triangular metallic sheets of Pd¹⁺ separated by insulating nonmagnetic layers of Co^{3+}O_6 edge-shared octahedra.

The above attributes, particularly the exceptional low- T mean-free path, and simple hexagonal Fermi surface, have enabled a remarkable string of recent achievements with bulk crystals of PtCoO_2 and PdCoO_2 . These include observations of: various forms of quantum oscillation^{14,15,28,29}, very large positive magnetoresistance along the c -axis³⁰, potential phonon-drag effects in resistivity¹⁵, possible hydrodynamic electron transport²⁸, and itinerant surface ferromagnetism^{26,31,32}. Yet more recently, non-local electrodynamics³³, directional ballistic transport³⁴, supergeometric electron focusing³⁵, and non-local transport³⁶ have been reported in PdCoO_2 crystals and micron-scale structures, exploiting the long mean-free-path and anisotropic Fermi surface. The addition of magnetic moments in PdCrO_2 adds further richness, encompassing magnetic frustration^{37–39}, a complex antiferromagnetic spin structure^{37–40}, possible chirality⁴⁰, an anomalous Hall effect^{41,42}, and T -linear resistivity^{43,44} potentially due to magneto-elastic scattering⁴⁴. Metallic delafossites are thus making their mark in condensed matter and materials physics, and potential applications are being explored, in nanoelectronic interconnects⁴⁵, harsh-environment electronic devices^{46–48}, electrocatalysis^{46,49}, ballistic transport devices^{34–36,46,47}, transparent conductors^{46,50}, terahertz sources⁵¹, etc.

Despite this progress, the origins of the ultrahigh conductivities and mean-free paths in metallic delafossites remain unclear. While progress has been made with understanding thermal properties of PdCoO_2 ¹⁸ and related phonon spectra^{52,53}, much remains to be elucidated regarding electron-phonon scattering and coupling⁵¹⁴ and thus the low room- T resistivities⁵. An important recent advance is a first-principles reproduction of the room-temperature resistivity and calculation of weak electron-phonon coupling constant in PdCoO_2 ²⁴. Yet more urgently given the above advances^{14,15,24,29,30,32–36}, the origin of the outstanding a - b -plane residual resistivities and low- T mean-free-paths remain incompletely understood^{5,46}. It is widely accepted that ultrahigh purity and ultralow defect density are necessary for such behavior^{5,14,15,28,54,55}, but, confusingly, the crystal growth methods applied to metallic delafossites^{6,14,16,56–59} are not typically capable of such^{5,54}. The prevailing method for PdCoO_2 and PtCoO_2 is a metathesis-based flux growth^{6,14,16,57,58}, which is not well understood, typically limited to ~ 1 -mm lateral sizes, and not performed under conditions that would be expected to realize ultrahigh purity. Multiple authors have in fact commented on the crude synthesis methods for metallic delafossites relative to other systems with comparable mean-free-paths^{5,54}. On the other hand, recent electron microscopy on single-crystal PdCoO_2 supports sufficiently low defect densities that only upper limits could be placed^{54,60}. An electronic transport study of metallic delafossites as a function of irradiation-induced point defect density also evidenced extraordinarily low initial defect densities on

the Pd/Pt planes, insensitive to the (unknown) disorder level on the B–O layers⁵⁴. It is thus unclear what the impurity and defect densities are in single-crystal metallic delafossites, how they are divided between A and B–O planes⁵⁴, if/how defect densities are minimized by current growth methods⁵⁴, or whether some form of defect mitigation or tolerance occurs⁵⁴. One proposal for the latter is the hidden kagome picture recently advanced to explain reduced electron-impurity scattering⁶¹.

The current work seeks to elucidate some of the above through advances that are thus far absent from the PdCoO_2 literature: improvements in bulk crystal growth in terms of mechanistic understanding, crystal size, defect density, and purity; more extensive structural and chemical characterization; and comprehensive trace impurity analysis. The latter is particularly conspicuous in its absence from the metallic delafossite literature, likely because the premier method—inductively coupled plasma mass spectrometry (ICP-MS)—typically involves acid digestion. Metallic delafossites such as PdCoO_2 and PtCoO_2 are unusually stable in extreme pH, however^{46–48}, likely hindering prior attempts at comprehensive trace impurity analysis.

Here, we first elaborate on a different crystal growth method for PdCoO_2 based on chemical vapor transport (CVT), for which a simple mechanism is proposed. CVT is then compared to the established metathesis/flux method and is shown to enable orders-of-magnitude gains in crystal size and mass, the highest structural quality yet reported, and record RRR. Nevertheless, particle-induced X-ray emission (PIXE) and low- T magnetometry suggest significant impurity concentrations. Enabled by microwave digestion methods, comprehensive trace impurity analyses of metathesis/flux-grown and CVT-grown PdCoO_2 crystals were thus performed by ICP-MS, with clear conclusions. Specifically, these metallic delafossite crystals are definitively *not* ultrapure in a general sense. Standard metathesis/flux crystals typically have ~ 250 ppm metals-basis impurities overall; CVT crystals are purer but still harbor ~ 50 ppm overall impurities. Through a detailed crystal-chemistry-based analysis, however, we show that the vast majority of these impurities must populate Co–O octahedral layers, while as few as four elements can conceivably substitute for Pd. The concentration of these elements is of order 1 ppm, ~ 100 times lower than the total impurity concentration, which is shown to be in quantitative agreement with the measured residual ρ_{ab} . We thus propose that a sublattice purification mechanism is central to the extraordinary low- T conductivity of metallic delafossites, enabling ultrahigh purity in the conductive Pd/Pt sheets, largely unaffected by substantial impurity concentrations in the CoO_6 octahedra.

Results

Chemical vapor transport crystal growth

As noted in the Introduction, metathesis-based flux growth has become standard for single-crystal PdCoO_2 and PtCoO_2 ^{6,14,16,57,58}. This is based on metathesis reactions such as $\text{PdCl}_2 + \text{Pd} + \text{Co}_3\text{O}_4 \rightarrow 2\text{PdCoO}_2 + \text{CoCl}_2$, *i.e.*, PdCl_2 , Pd, and Co_3O_4 reagents (99.995–99.999% purity in our case) reacting to form the target PdCoO_2 plus a CoCl_2 by-product, which is chemically removed (see Methods for more details). In the current study, dwell temperatures of 700–750 °C were employed for metathesis growth, followed by cooling to 400 °C at 40–60 °C/h. As shown in the scanning electron microscopy (SEM) image in Fig. 1b, the resulting product is a mass of PdCoO_2 crystals and crystallites. The optical microscope image in the inset to Fig. 1b highlights one of the largest crystals from a typical growth, measuring $0.8 \times 0.6 \text{ mm}^2$ laterally, and 0.017 mm thick. This corresponds to 0.008 mm^3 and 0.065 mg, comparable to literature reports^{16,28,34,54,55}. Typical powder X-ray diffraction (PXRD) data from such crystals are shown in Fig. 1d (green), displaying a good match with a PdCoO_2 standard (gray), and yielding lattice parameters $a = 2.8308 \pm 0.0002 \text{ \AA}$ and $c = 17.747 \pm 0.002 \text{ \AA}$, in agreement with accepted values^{5,6}.

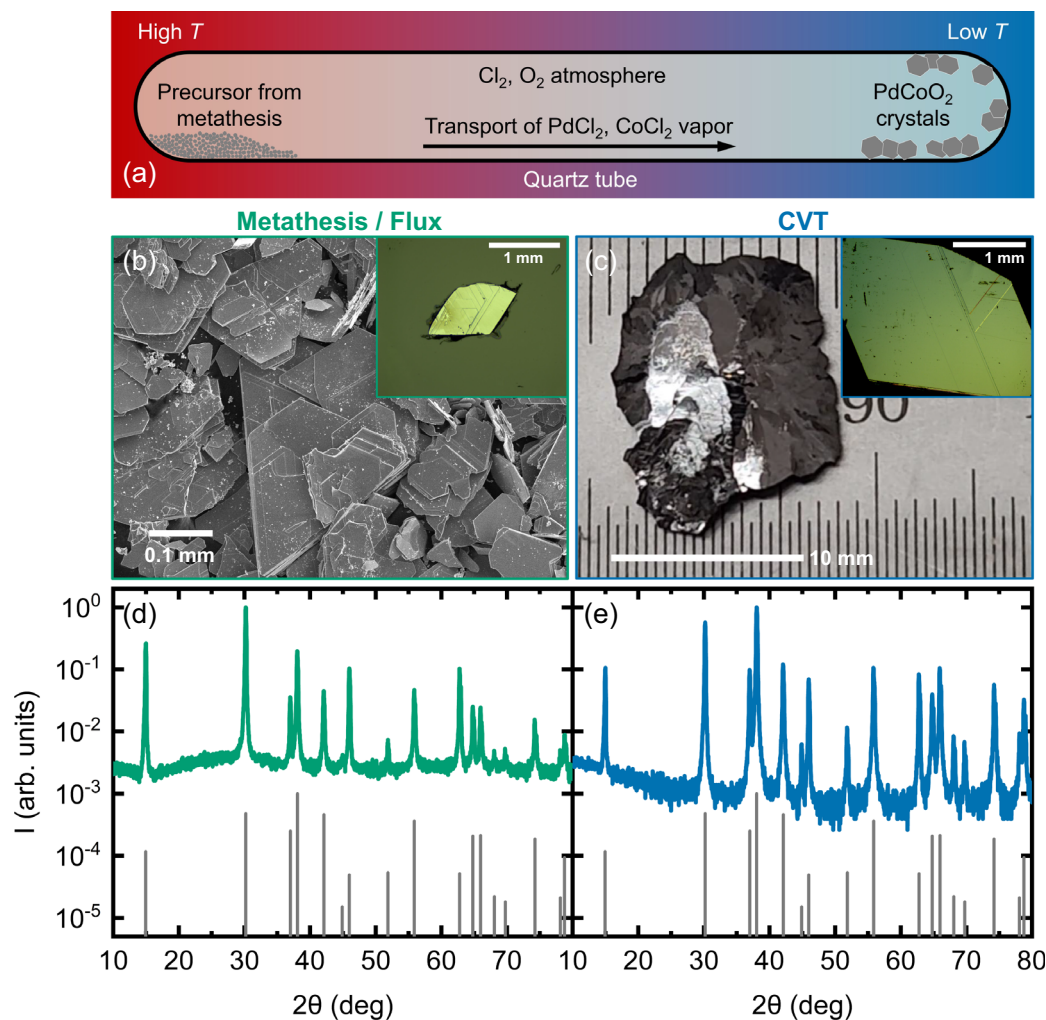


Fig. 1 | Crystal growth, microscopy, and powder X-ray diffraction for metathesis/flux and chemical vapor transport (CVT) crystals. **a** Schematic of CVT growth of PdCoO₂. **b** Scanning electron microscopy image of the products of metathesis/flux growth. Inset: Optical microscopy image of a larger single crystal from metathesis/flux growth (0.8 × 0.6 × 0.017 mm³). **c** Optical microscopy image

of a multicrystal from CVT growth. Inset: Optical microscopy image of a typical single crystal from CVT (3.5 × 2.0 × 0.17 mm³). **d, e** Powder X-ray diffraction patterns (intensity vs. 2θ angle) from representative ground crystals from the metathesis/flux ((**d**), green) and CVT ((**e**), blue) methods; reference patterns are shown in gray.

While such crystals have enabled exciting advances^{14,15,17,25–30,32–36}, as discussed in the Introduction, it is nevertheless true that little progress in PdCoO₂ crystal size or quality has been reported since ca. 2007. There is also limited understanding of the growth mechanism. Most publications describe the mechanism as “flux” or “self-flux” and employ specific temperature-time trajectories but with little explicit justification^{14,16,56–58}. Seeking improvement over this, we explored CVT crystal growth of PdCoO₂. CVT is not commonly applied to complex oxides but the fact that PdCoO₂ decomposes (at ~800 °C in air, for example⁴⁸) hints at CVT as a possibility, as does the relatively low decomposition temperature of PdCl₂ (~600 °C in low Cl₂ partial pressure^{62,63}), a potential transport agent. CVT was thus performed in a set-up shown schematically in Fig. 1a, and elaborated upon in Methods and Supplementary Notes 1 and 2 (Supplementary Figs. 1–3 and Supplementary Tables 1 and 2). The solid precursors are coarse PdCoO₂ powder derived from the above metathesis growth, along with 99.999%-pure PdCl₂. At typical hot and cold-zone temperatures of 760 and 710 °C, we propose that PdCl₂ decomposition is followed by a reaction such as PdCoO₂(s) + 2Cl₂(g) ⇌ PdCl₂(g) + CoCl₂(g) + O₂(g), *i.e.*, Pd chloride and Co chloride vapor transport across the temperature gradient in a Cl₂(g) and O₂(g) atmosphere. The reaction runs to the left in the growth (cold) zone, resulting in PdCoO₂ crystals

and chloride by-products, which are chemically removed (see Methods).

As shown in Fig. 1c, after optimization of hot and cold-zone temperatures, relatively large PdCoO₂ crystals and multicrystals derive from this process, at high yield (>90%). Specifically, the reaction product is a mix of single crystals and larger multicrystals, the latter likely forming due to nucleation of Pd or PdO seeds during the initial inverted-temperature-gradient period of the growth (see “Methods” section and Supplementary Note 1). Multicrystals up to 12 × 12 mm² laterally and 0.3 mm thick are grown (Fig. 1c), corresponding to 43.2 mm³ and 345 mg. Gently breaking apart such multicrystals isolates single crystals up to 6.0 × 4.0 mm² laterally and 0.17 mm thick, corresponding to 4.08 mm³ and 32.6 mg. A representative example is shown in the inset to Fig. 1c. These CVT PdCoO₂ multicrystals are thus larger than our metathesis/flux crystals by factors of ~15 in maximum lateral dimension, ~18 in thickness, and ~5300 in volume and mass. Correspondingly, the CVT single crystals are larger than metathesis/flux single crystals by factors of ~8 in maximum lateral dimension, ~10 in thickness, and ~500 in volume and mass.

As illustrated in Fig. 1e, PXRD patterns from powdered CVT crystals are also consistent with single-phase PdCoO₂, with $a = 2.8306 \pm 0.0002$ Å and $c = 17.746 \pm 0.002$ Å. Intriguingly, large-scale

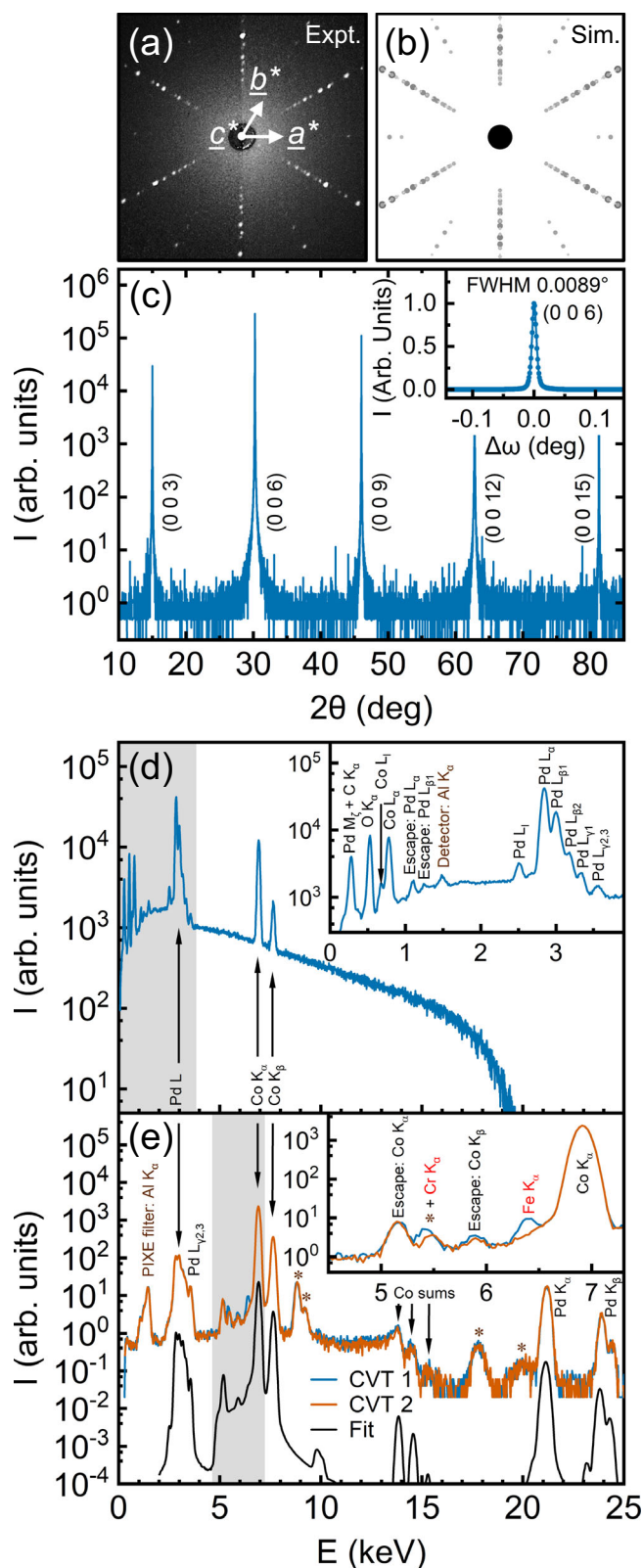


Fig. 2 | Structural and chemical characterization of CVT-grown single-crystal PdCoO₂. **a** Back-reflection Laue X-ray diffraction pattern along a [001] zone axis of a representative single crystal, with reciprocal-space axes labeled. **b** Corresponding simulated Laue pattern where the size of the points indicates their relative intensity and the central black circle represents the beam aperture. The simulation is based on the accepted PdCoO₂ structure and lattice parameters^{6,79}. **c** Specular high-resolution X-ray diffraction (intensity vs. 2θ angle) from a representative 001-oriented single crystal, showing only 00 l reflections. Inset: Rocking curve through the 006 reflections in (c), with a full-width-at-half-maximum (FWHM) of 0.0089°. **d** Energy-dispersive X-ray spectrum (intensity vs. energy) from a representative region ($25 \times 25 \mu\text{m}^2$) of a single crystal. The peaks are labeled and the inset is a close-up of the 0 to 3.9 keV region shaded gray. **e** Particle-induced X-ray emission spectra from two crystals (CVT 1 in blue and CVT 2 in orange), along with the GUPIXWIN simulation result discussed in the text (black, vertically offset for clarity). The peaks labeled with an “*” are known instrumental artifacts in our ion beam accelerator/PIXE system. The inset is a close-up of the 4.5–7.3 keV region shaded gray; note the different intensities of the Cr and Fe K α peaks in the two crystals. The Cr peak at 5.4 keV has partial overlap with an artifact peak but the variation in intensity from crystal to crystal strongly suggests a contribution from Cr. The Fe peak at 6.4 keV has no such overlap and also varies from crystal to crystal.

parameters are lower is in fact supported by *t*-testing, which indicates null-hypothesis *p* values below 0.0001 for both *a* and *c*, far below often-used confidence cutoffs such as *p* = 0.01. The smaller standard deviation indicates better reproducibility with CVT, while decreased cell volume often indicates lower defect density^{64–69}, including in complex oxides^{65–69}. Minimization of unit cell volume has in fact emerged as a guiding principle for the synthesis of highly perfect complex oxides with minimized densities of non-stoichiometry-accommodating defects^{65–69}. These data thus hint at lower defect densities in CVT-grown crystals, a conclusion that is reinforced below. As a final comment on structure, note that powdered samples of these CVT crystals were recently used in a 12–1000 K structural study *via* PXRD and accompanying refinement, confirming their single-phase nature and the thermal stability of the *R* $\bar{3}m$ structure¹⁸.

Structural and chemical characterization

With CVT growth established to provide substantial improvements in PdCoO₂ crystal size and mass, and with improved defect density suggested by the lattice parameters, it is important to more rigorously assess structural quality and purity. Preliminary prior characterization established single crystallinity *via* two-dimensional single-crystal X-ray diffraction¹⁸. In Fig. 2a this is improved on by presenting Laue diffraction data conclusively confirming single crystallinity. The six-fold-symmetric pattern of diffraction spots down this [001] zone axis, interspersed with a second six-fold pattern of weaker spots (seen upon close examination of Fig. 2a), is as expected, as illustrated by the simulated pattern in Fig. 2b based on the accepted *R* $\bar{3}m$ structure and lattice parameters⁶. Wide-range specular high-resolution X-ray diffraction (HRXRD) was also performed on 001-oriented crystals (Fig. 2c), showing only sharp 003 through 0015 reflections, further confirming single crystallinity and phase purity. Of particular significance, a HRXRD rocking curve through the 006 reflection is shown in the inset to Fig. 2c, revealing a full-width-at-half-maximum of only 0.0089°. To the best of our knowledge, this is the lowest rocking curve width reported for a metallic delafossite, demonstrating very low mosaic spread, another strong indicator of low defect density.

Turning to chemical characterization, Fig. 2d shows an energy-dispersive X-ray spectroscopy (EDS) scan from a representative PdCoO₂ CVT crystal. Only Pd *L* and Co *K* peaks are clearly visible in this wide-energy-range scan, their relative intensities giving a Pd/Co ratio of 0.98 ± 0.05, consistent with the nominal stoichiometry. The inset to Fig. 2d focuses on the low-energy region shaded gray in the main panel, revealing, with the exception of a small detector-artifact peak and the

comparisons of the lattice parameters for flux/metathesis and CVT crystals suggest subtle but significant differences. Averaged overall measured crystal batches (*n* = 26 for metathesis/flux and *n* = 18 for CVT), our metathesis flux crystals have *a* = 2.83088 ± 0.00078 Å, *c* = 17.7495 ± 0.0047 Å (where the uncertainties are now standard deviations), while CVT crystals have *a* = 2.83013 ± 0.00023 Å, *c* = 17.7446 ± 0.0018 Å. Both the lattice parameters and standard deviations are therefore lower in CVT crystals. That the lattice

inevitable C contamination in SEM/EDS, only peaks from Pd, Co, and O. Unsurprisingly, EDS is thus not sufficiently sensitive to detect any trace impurities in these PdCoO₂ crystals, which was the motivation for the PIXE data in Fig. 2e. PIXE is analogous to EDS except that the excitation is achieved with MeV-range He ions rather than electrons, vastly decreasing the broad background due to bremsstrahlung. As can be seen in Fig. 2e, which shows spectra from two different CVT crystals (orange and blue), PIXE thus exposes a plethora of Pd, Co, and sum peaks, at a high signal-to-noise ratio. Aside from some instrumentation artifacts (labeled with asterisks in Fig. 2e), almost all aspects of these spectra are reproduced by a GUPIXWIN⁷⁰ simulation for PdCoO₂, shown as the black line. The inset to Fig. 2e, however, shows a close-up of the 4.5–7.3 keV region (shaded gray in the main panel), highlighting two peaks that are not accounted for by Pd, Co, or O. These peaks also exhibit crystal-to-crystal variations in intensity, strongly suggesting that they derive from trace impurities. The ~5.4 keV peak very likely indicates Cr impurities, while the 6.4 keV peak is very likely due to Fe. Full quantification of impurity concentrations at this level is challenging for PIXE but our best estimates based on GUPIXWIN fits to Pd *L*, Co *K*, and Fe *K* peaks suggest Fe concentrations of ≥ 50 ppm. (As for all impurity concentrations in this paper, this value is on a weight basis, *i.e.*, it is in $\mu\text{g/g}$). While this is only approximate, this is our first indication that even CVT-grown PdCoO₂ crystals may not actually be ultrapure. As a final comment on these PIXE data, we note that Cl was not detected; the estimated limit of detection is of order 1000 ppm, however, due to the overlap of Cl *K* and Pd *L* peaks.

Electronic and magnetic properties

Electronic transport is an excellent relative probe of total defect and impurity densities, and thus *T*-dependent ρ_{ab} measurements were made

on our CVT-grown crystals. It is essential to acknowledge at this point that such measurements are nontrivial for single-crystal PdCoO₂^{17,28,54,57}, because of the extremely small low-*T* resistances (due to the very low residual ρ_{ab}), and the sizable *c*-axis/*a*-*b* plane resistivity anisotropy (~350–750, depending on *T*^{8,14–16}). The most accurate measurements in the literature in fact use focused-ion beam techniques to pattern structures with long channel lengths to increase resistance, at the same time fully constraining the current path in the *a*-*b* plane^{17,28,54,57}. In our case, the availability of larger crystals than in prior work enabled cleavage into relatively long and thin bar-shaped samples for simpler, in-line, top-contact, four-wire measurements. The inset to Fig. 3a shows an example of such an in-line geometry on a 1.2-mm-long, 23- μm -thick crystal. Even in this case, residual resistances were found to be $\sim 20 \mu\Omega$, necessitating low-noise measurements and careful accounting for instrumental offset voltages. Full details are provided in Methods and Supplementary Note 3 (including Supplementary Figs. 4–6 and Supplementary Tables 3–5). Briefly, an AC resistance bridge with a pre-amplifying channel scanner was employed, using parallel measurements on superconducting *V* thin films to determine and account for offsets. Top-contact geometries such as those shown in the inset to Fig. 3a are also subject to systematic error due to the large ρ_c/ρ_{ab} ^{8,14–16}. As described in Supplementary Note 3, finite-element simulations of current flow and potential drop were thus performed in our specific measurement geometry. These confirm overestimation of ρ_{ab} due to the large ρ_c that generates potential drop through the crystal thickness. This issue worsens with cooling (as ρ_c/ρ_{ab} increases), meaning, importantly, that RRR values in this geometry represent lower bounds on true values (see Supplementary Note 3 for details).

Based on the above procedures, presented in Fig. 3a is $\rho_{ab}(T)$ for the representative CVT-grown PdCoO₂ crystal shown in the inset;

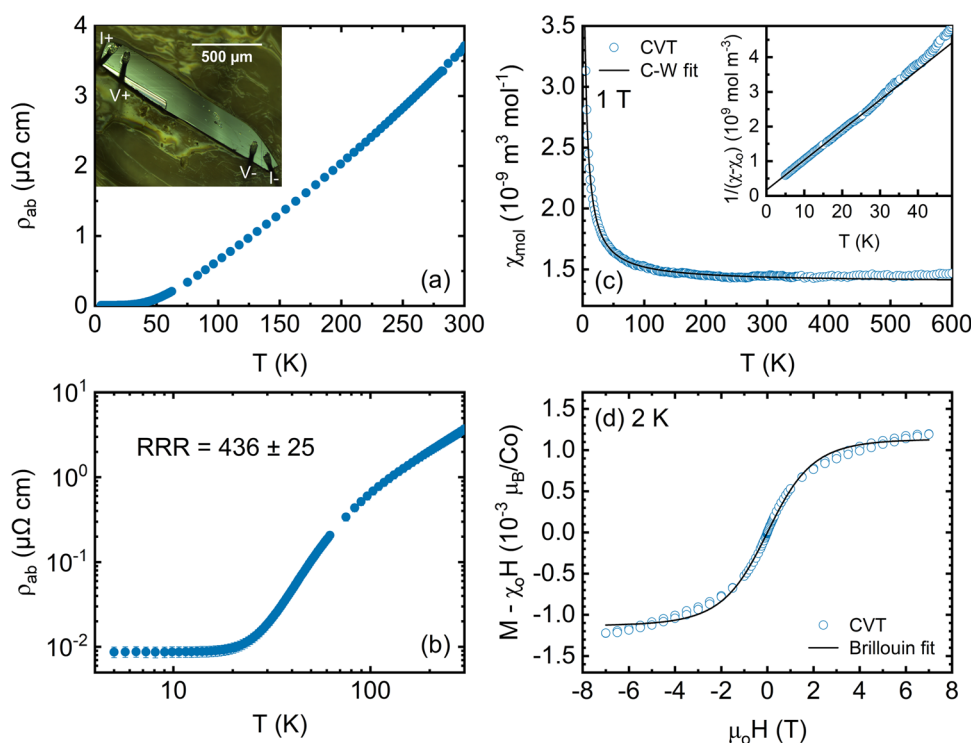


Fig. 3 | Electronic and magnetic properties of CVT-grown single-crystal PdCoO₂. **a** *a*-*b*-plane resistivity (ρ_{ab}) vs. temperature (*T*) on a representative single crystal. Inset: Image of the crystal and four-point in-line contact arrangement. **b** Data from (a) on a \log_{10} - \log_{10} scale, highlighting the residual resistivity ratio of 436 ± 25 . The error bars in (b) represent the uncertainty estimated from offset subtraction (dominant at low-*T*) and sample dimension measurements. **c** Molar magnetic susceptibility (χ_{mol}) vs. *T* in a 1 T magnetic field (blue open circles), from a

representative powdered crystal. The black solid line is a fit to a sum of Pauli and Curie-Weiss susceptibilities, as discussed in the text. Inset: *T* dependence of $(\chi_{\text{mol}} - \chi_0)^{-1}$, where χ_0 is the *T*-independent susceptibility. The solid black line is a 5–20 K Curie-Weiss fit. **d** 2-K magnetization (*M*, corrected for χ_0) vs. magnetic field ($\mu_0 H$) for the crystal in (c) (blue open circles). The solid black line is a Brillouin fit described in the text.

Fig. 3b shows the same data on a \log_{10} - \log_{10} scale. The 300 K resistivity of this representative crystal is $3.65 \mu\Omega\text{cm}$, which can be compared to reported values of 2.0 – $6.9 \mu\Omega\text{cm}$ using standard contact methods^{8,14–16} and $3.1 \mu\Omega\text{cm}$ using more accurate focused-ion-beam-patterned geometries¹⁷. Our value of $3.65 \mu\Omega\text{cm}$ is thus indeed slightly larger than the most accurate determination of $3.1 \mu\Omega\text{cm}$ ¹⁷, but within the bounds expected for overestimation of ρ_{ab} due to the top-contact geometry (see Supplementary Note 3). On cooling, the $\rho_{\text{ab}}(T)$ of this crystal saturates below 10 – 20 K, reaching a measured value of $8 \text{ n}\Omega\text{cm}$. Taking this at face value, and considering the residual resistivity measurement uncertainty (dominated by offset subtraction), a RRR of 436 ± 25 is indicated. As noted above and discussed in detail in Supplementary Note 3, however, this RRR represents a lower bound due to the top-contact geometry. Finite-element simulations suggest a true residual ρ_{ab} of $\sim 4.4 \text{ n}\Omega\text{cm}$, yielding an actual RRR up to ~ 670 (see Supplementary Note 3). Even without this correction, however, our measured RRR of ~ 440 is a record in PdCoO_2 , which can be compared to 376 in prior metathesis/flux-grown crystals measured with focused-ion-beam patterning methods¹⁷ (or 407 based on less accurate contacting methods¹⁴). In addition to realizing order-of-magnitude gains in crystal size and mass, our CVT approach thus also results in measurably lower disorder in electronic transport.

Magnetometry measurements provide another probe of crystal quality and impurity concentrations in PdCoO_2 and were thus performed on CVT crystals. A typical result for the T -dependent molar susceptibility (χ_{mol}) is shown in Fig. 3c. As illustrated by the black solid line, these data are well described by $\chi_{\text{mol}}(T) = \chi_0 + C/(T - \theta)$, *i.e.*, a sum of T -independent Pauli-related and T -dependent Curie-Weiss contributions, where C is the Curie constant and θ is the Curie-Weiss temperature. The Pauli contribution derives from delocalized Pd d electrons, the $\chi_{\text{Pauli}} = \frac{3}{2}\chi_0 = 1.65 \times 10^{-4} \text{ emu mol}^{-1} \text{ Oe}^{-1}$ (the factor of $3/2$ accounts for Landau diamagnetism) in this case being near the middle of the distribution of literature values (0.9×10^{-4} to $2.9 \times 10^{-4} \text{ emu mol}^{-1} \text{ Oe}^{-1}$, see Table 1). The low- T Curie-Weiss tail, however, which should not ideally occur in PdCoO_2 (the Co^{3+} ions are low-spin, $S = 0$), very likely arises from local moments due to magnetic impurities. As shown in Table 1, the $\theta = -2.6$ K extracted from the fit in Fig. 3c is indeed small, indicating weak inter-moment interactions, as would be expected of dilute impurities. This is reinforced by the inset to Fig. 3c, where $(\chi_{\text{mol}} - \chi_0)^{-1}$ is plotted *vs.* T , the 5 – 20 K fit yielding $\theta = -2.0$ K.

Interestingly, the Curie constant extracted from the fit in Fig. 3c yields an effective number of Bohr magnetons (μ_{eff}) as high as $0.09 \mu_{\text{B}}$ per formula unit (Table 1). Further insight into this is provided in Fig. 3d, which shows the applied magnetic field (H) dependence of the

magnetization (M) at 2 K, after correcting for χ_0 . The solid black line Brillouin fit captures the data moderately well, yielding a reasonable $J = 1.2$, along with a concentration of local moments corresponding to ~ 130 ppm. (This is again on a weight basis; the atomic mass of Fe was assumed to convert from a number density-of-impurities (from the fit in Fig. 3d) to a weight-basis concentration). Taking this J and combining it with the Curie constants from the fits in Fig. 3c then yields local moment concentrations of ~ 200 ppm. The low- T paramagnetism in Fig. 3c, d, can thus be consistently described by dilute, non-interacting local atomic moments, at concentrations of order 100 ppm. While some fraction of this Curie-tail magnetism no doubt arises from surface contamination, this is a second indication, along with PIXE data (Fig. 2e), that even CVT-grown PdCoO_2 crystals host substantial impurity concentrations. Nevertheless, the μ_{eff} values from the Curie-Weiss tails of CVT-grown crystals do represent a significant improvement over metathesis/flux crystals. This is emphasized in Table 1, which includes data from our metathesis/flux crystals, in addition to prior literature^{14,16,58}. The Curie-Weiss μ_{eff} of our CVT crystals is over 4 times lower than our metathesis/flux crystals and is the lowest reported for PdCoO_2 . Literature values on metathesis/flux-grown crystals in fact span 0.15 – $0.78 \mu_{\text{B}}$ per formula unit (Table 1)^{14,16,58}, implying substantial magnetic impurity concentrations, even in crystals with large RRR¹⁴. This apparent contradiction—clear indications of significant densities of magnetic impurities from magnetometry, in crystals that exhibit low disorder in transport—appears not to have been addressed in the literature. While CVT crystals are improved in this regard (they have the lowest μ_{eff}), and surface contributions are likely, the implied level of magnetic impurities is concerning. For this reason, and to augment the chemical characterization in Fig. 2d, e, we thus undertook trace impurity analysis *via* ICP-MS.

Impurity analysis

As alluded to in the Introduction, ICP-MS-based trace impurity analysis on PdCoO_2 is complicated by the extraordinary acid etch resistance of metallic delafossites^{46–48}, which hinders simple acid digestion. We thus employed microwave digestion techniques (see Methods for details), achieving complete digestion in ~ 15 bar of aqua regia or concentrated nitric acid vapor at 200 °C. ICP-MS was then performed on both metathesis/flux and CVT PdCoO_2 , quantifying the concentrations of 54 selected elements in a metals-basis approach (see Methods and Supplementary Note 4). This led to the immediate conclusion, contrary to the naïve view, that PdCoO_2 crystals are *not* generally ultrapure (Table 2). Averaged over multiple crystals and ICP-MS runs, the total metals-basis impurity concentration in our metathesis/flux crystals is in fact 251 ± 3 ppm (Table 2). We emphasize that this value derives from the same synthesis method used in many prior reports on PdCoO_2 ^{5–8,14–17,25–30,32–36,54,55,58,60} with ρ_{ab} down to $8 \text{ n}\Omega\text{cm}$ and RRR up to 376 ¹⁷. Our CVT crystals are purer, as might be expected of vapor-based growth, but still retain an average overall metals-basis impurity concentration of 47 ± 8 ppm (Table 2).

Such substantial impurity concentrations, which are broadly consistent with PIXE and magnetometry (Figs. 2e and 3c, d), frame a central question for the remainder of this work: How can the record residual ρ_{ab} of these materials, and their exceptional RRR, be reconciled with such impurity concentrations? To underscore the importance of this question, note that the reported 20 - μm low- T mean-free path of PdCoO_2 would require impurity concentrations several orders-of-magnitude lower than the above ICP-MS values, a point that we return to quantitatively below. Analysis of the distribution of the detected impurity elements casts much light on this issue. To this end, we first elaborate a simple classification scheme for the various substitutional elemental impurities that can be accommodated in PdCoO_2 . Figure 4a depicts the crystal structure of PdCoO_2 , along with a classification for potential A- and B-site impurities in the ABO_2 delafossite structure. The critical point here is that, very unlike ABO_3 perovskites

Table 1 | Summary of parameters from analysis of magnetometry data on PdCoO_2 crystals in this work and in prior literature

Reference	Measurement details	χ_0 (emu mol ⁻¹ Oe ⁻¹)	θ (K)	μ_{eff} (μ_{B} /formula unit)
Tanaka et al. ¹⁶	Ground crystal	1.9×10^{-4}	-3.50	0.66
Tanaka et al. ¹⁶	$H \perp c$	1.1×10^{-4}	10.63	0.69
Tanaka et al. ¹⁶	$H \parallel c$	1.6×10^{-4}	0.69	0.57
Tanaka et al. ⁵⁸	Ground crystal	0.6×10^{-4}	-12.13	0.78
Takatsu et al. ¹⁴	$H \perp c$	1.9×10^{-4}	-38.9	0.20
Takatsu et al. ¹⁴	$H \parallel c$	1.7×10^{-4}	-40.8	0.15
This work, metathesis/flux	Ground crystal	2.0×10^{-4}	-8.1	0.37
This work, CVT	Ground crystal	1.1×10^{-4}	-2.6	0.09

Shown are the literature reference, measurement details, temperature-independent susceptibility (χ_0), Curie-Weiss temperature (θ), and effective number of Bohr magnetons from the low-temperature Curie-Weiss contribution (μ_{eff}). Note that the Pauli susceptibility can be calculated using $\chi_{\text{Pauli}} = \frac{3}{2}\chi_0$, as discussed in the text.

Table 2 | Summary of average impurity concentrations (in weight-basis ppm) in metathesis/flux- and CVT-grown PdCoO₂ crystals, as determined by ICP-MS

Total Impurities in PdCoO ₂						
	Known A-site ABO ₂ , fits Pd site PdCoO ₂ (μg/g)	Known A-site ABO ₂ , does not fit Pd site PdCoO ₂ (μg/g)	Fits Co site, PdCoO ₂ (μg/g)	Known B site ABO ₂ , does not fit Co site PdCoO ₂ (μg/g)	All other (μg/g)	Total (μg/g)
Flux	4.41 ± 0.03	21 ± 2	132 ± 2	67 ± 1	27.3 ± 0.5	251 ± 3
CVT	1.9 ± 0.3	0.4 ± 0.1	42 ± 7	0.6 ± 0.2	1.9 ± 0.6	47 ± 8

The averages are over 2–3 runs on 1–3 crystals, and the uncertainties listed are standard deviations. Na, B, and Si, which are common glassware impurities, were excluded from all analyses. First column: Total concentrations of elements known to adopt the A-site in ABO₂ compounds that also fit the Pd site in PdCoO₂. Second column: Total concentrations of elements known to adopt the A-site in ABO₂ compounds that do not fit the Pd site in PdCoO₂. Third column: Total concentrations of elements that fit the Co site in PdCoO₂. Fourth column: Total concentrations of elements known to adopt the B-site in ABO₂ compounds that do not fit the Co site in PdCoO₂. Fifth column: Concentration of all other elements measured (i.e., those not in columns 1–4). Sixth column: Total of all prior columns.

for example, there is a massive asymmetry in the number of elements that can conceivably populate A *vs.* B sites. This arises because the B-site in metallic ABO₂ delafossites involves a common cation valence in oxides (3+) and a common coordination with O²⁻ (octahedral); this is as in perovskites, which can accommodate much of the periodic table on the B site. The A-site in metallic ABO₂ delafossites, on the other hand, involves a relatively uncommon valence in oxides (1+) and a far less common coordination with O²⁻ ions (linear, see the structure in Fig. 4a). This situation, which contrasts starkly with ABO₃ perovskites, greatly reduces the possible accommodation of A-site *vs.* B-site substitutional impurities in ABO₂ compounds.

Considering this in more detail, as shown in Fig. 4a, potential A-site-substituting impurities can be classified in terms of elements that are known to adopt the A-site in ABO₂ compounds, that either can (dark yellow) or cannot (light yellow) feasibly substitute for Pd in PdCoO₂. We determine this feasibility by applying Goldschmidt-type criteria, requiring <30% ionic size mismatch, an ability to adopt the required coordination, and valence within ± 1 of the host element. Figure 4b then shows a periodic table of select elements most relevant to ABO₂ compounds, labeled with their valence, coordination number, and ionic radii in the state most closely matching the delafossite structure. As shown in the figure, Li⁺, Na⁺, K⁺, Rb⁺, Cu⁺, Ag⁺, Pt⁺, and Hg²⁺ (shaded yellow) are known to adopt the A-site in ABO₂ compounds, but in most cases cannot feasibly substitute for Pd in PdCoO₂. In particular, Li⁺, Na⁺, K⁺, and Rb⁺ (light yellow) only form ABO₂ compounds with distinctly different structure to delafossite PdCoO₂, with large coordination number with O²⁻. In most cases their ionic radii in this coordination are also far beyond the 30% mismatch for feasible substitution for Pd. In fact, the elements that can feasibly substitute for Pd in PdCoO₂ (dark yellow) number only four: Cu, Ag, Pt, and Hg, highlighted via the bold border in Fig. 4b. Hg substitution would also be a special case, as the 2+ valence (Hg does not typically adopt 1+ valence in 2-fold coordination) would require an additional charge-balancing defect. This general concept is supported by prior work on deliberately Mg-substituted PdCoO₂, where A-site substitution with Mg²⁺ was argued against based on similar reasoning⁷¹.

The situation on the B site is very different. As shown in Fig. 4a, potential B site substituents can be classified in terms of those that are known to adopt the B site in delafossites and can feasibly substitute for Co (darkest blue), those that are known to adopt the B site in ABO₂ compounds but cannot feasibly substitute for Co (lightest blue), and those for which it is unknown whether they form ABO₂ compounds but do fit the Co site in PdCoO₂ (intermediate blue). Again, feasibility is based on <30% size mismatch, 3 ± 1 valence, and octahedral coordination. As shown in Fig. 4b, the total group of possible B-site substituents is numerous, totaling at least 40 (all blue shades), remaining as high as 20 even after applying our fit criteria (darkest blue shades). In contrast to ABO₃ perovskites, the fundamental crystal chemistry of the ABO₂ delafossites thus results in a large asymmetry between the number of elements that can exist as substitutional impurities on the A and B sites.

Figure 4c next maps the measured average concentrations of various ICP-MS-detected elements in CVT-grown PdCoO₂ crystals onto the classification scheme in Fig. 4a, b. This periodic table employs the log₁₀ color scale of average impurity concentrations shown to the right, also labeling the concentration and limit of detection beneath each element. The conclusion is simple. Substantial concentrations are found of elements that are likely to populate the Co site in PdCoO₂ (e.g., Mn, Fe, Ni, Al, Cr, Ir, Sn; the darker blue shades in Fig. 4b), but not of elements that can feasibly populate the Pd site. Neither Cu, Ag, Pt, or Hg (in the dark border in Fig. 4b, c) reach even 1 ppm in CVT crystals. These findings are further quantified in Tables 2–4, where Table 2 summarizes the total impurity concentrations of the elements likely to populate the Pd and Co sites in PdCoO₂. In metathesis/flux crystals, of the total impurity concentration of 251 ppm (far right, Table 2), at least 132 ppm are elements that would be expected to populate the Co site (darkest blue shades in Fig. 4b), whereas only 4.4 ppm are elements that could feasibly populate the Pd site (Cu, Ag, Pt, Hg, dark yellow in Fig. 4b). We thus define a sublattice purification ratio of 4.4/251 = 1.8% of the total impurity concentration that could feasibly substitute for Pd. As also shown in Table 2, the equivalent for CVT PdCoO₂ is 1.9/47 = 4.0% of the total average impurity concentration that could feasibly substitute for Pd, in this case only 1.9 ppm.

Tables 3 and 4 break these concentrations down further, into the only four elements that can feasibly populate the Pd site (Table 3) and the most prevalent elements likely to populate the Co site (Table 4). The former group consists of only Ag, Hg, Cu, and Pt, while the latter group includes Al, Cr, Mn, Fe, and Ni. Notable here is that one of the largest differences between CVT and metathesis/flux crystals is the decrease in Al, possibly due to the high thermal stability and low volatility of Al oxides. Another difference is the non-negligible concentration of impurities in metathesis/flux crystals that are not obviously capable of populating either the A or B sites. Surface contamination, strained B-site accommodation, and uptake in the minor impurity phases sometimes detected in metathesis/flux crystals (see Supplementary Fig. 3a and associated discussion) can likely account for this. The concentrations of Cr, Mn, Fe, and Ni are also of particular interest, due to their likely magnetic character, no doubt contributing to the Curie-Weiss susceptibility in Fig. 3c, d, and Table 1. Quantitatively, the estimated magnetic impurity concentration from Table 4 is 31 ppm in CVT crystals, compared to order 100 ppm from magnetometry. This is reasonable agreement considering the likelihood of additional surface contamination in magnetometry. In terms of comparisons to PIXE, ICP-MS on CVT crystals indicates 9 ± 2 ppm of Fe, also comparing reasonably to the order-50-ppm approximate estimate from PIXE (Fig. 2e). Finally, ICP-MS was also used to determine the Pd/Co ratio of CVT crystals, yielding 1.08 ± 0.02. This is inconsistent with the EDS result of 0.98 ± 0.05 at first sight, but EDS data were acquired from 25 × 25 μm² regions free of surface particles. These particles are of course not excluded from ICP-MS, and thus remnant surface Pd and PdCl₂ likely skews the ICP-MS Pd/Co ratio.

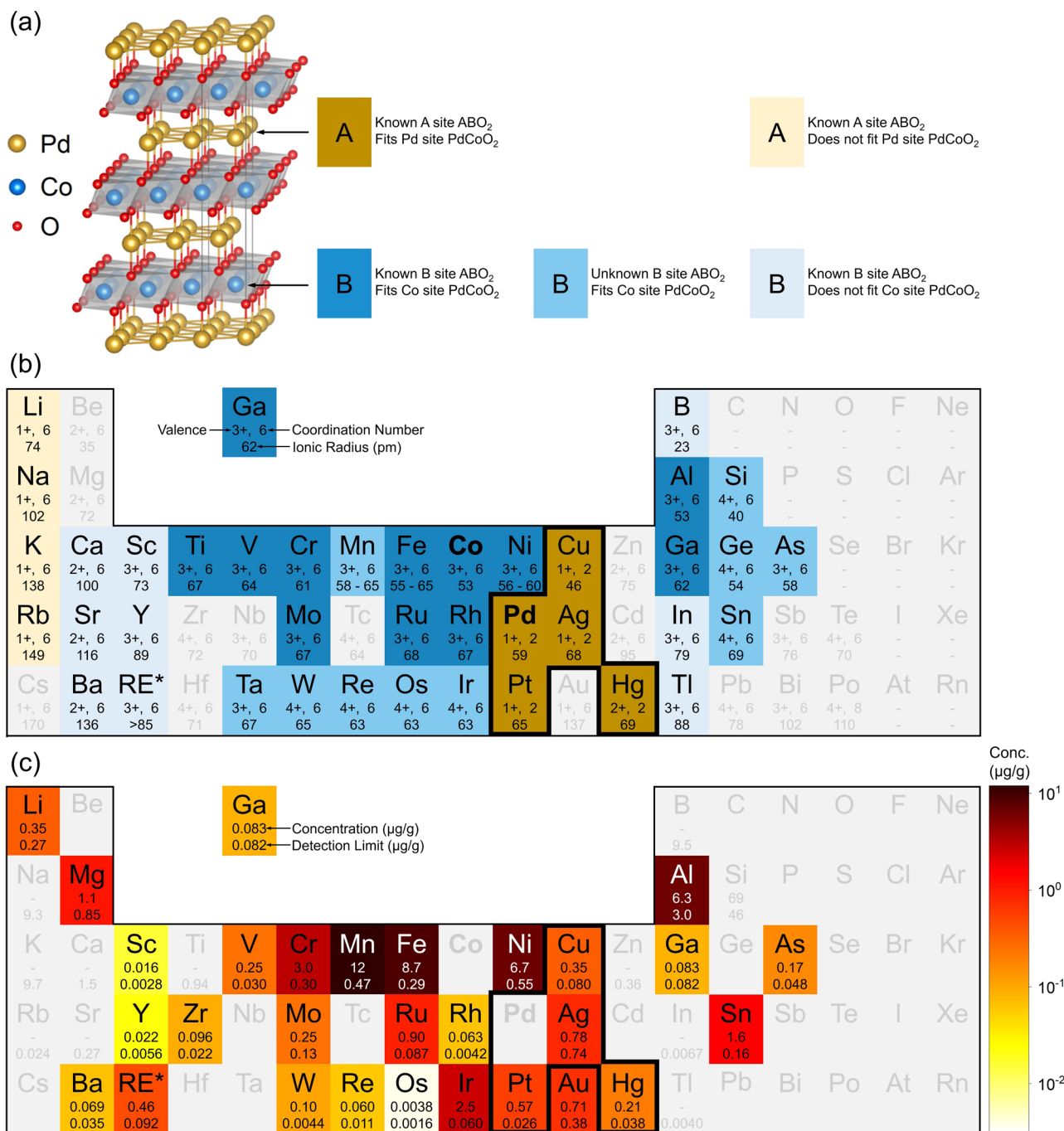


Fig. 4 | Impurity analysis of CVT-grown $PdCoO_2$. **a** $PdCoO_2$ crystal structure. **b** Periodic table highlighting elements relevant to the delafossite structure. As in (a), light yellow highlights elements that are known to adopt the A-site in ABO_2 compounds but do not fit the Pd site in $PdCoO_2$. Dark yellow highlights elements that are known to adopt the A-site in delafossites and do fit the Pd site in $PdCoO_2$; these are highlighted by the bold black border. Analogously, the lightest blue highlights elements that are known to adopt the B site in ABO_2 compounds but do not fit the Co site in $PdCoO_2$, and the darkest blue highlights elements that are known to adopt the B site in delafossites and do fit the Co site in $PdCoO_2$; the intermediate blue shade highlights elements for which it is unknown whether they adopt the B site in ABO_2 compounds but they do fit the Co site in $PdCoO_2$. In this scheme, dark yellow highlights elements likely to substitute for Pd (only four), while the two darker blue colors highlight elements likely to substitute for Co (>20). Also

shown for each element are the valence, coordination number, and ionic radius⁸⁰ in the state most closely relevant to delafossite oxides. (Ranges of radii are for low- to high-spin states). Au is not shaded dark yellow in (b); there exists some evidence of Au^{1+} in linear coordination with O^{2-} ⁸¹ but it is uncommon. **c** Periodic table labeled with the detected concentration and detection limit for each element probed in mass spectrometry. All values are weight-basis ppm, averaged over multiple runs and CVT crystals, as in Tables 2–4. The color scale (right) is a \log_{10} -scale of average impurity concentration in CVT crystals. As in (b), the bold black border highlights elements likely to substitute for Pd; their total concentration is only 1.9 ppm. The entire rare-earth element block appears as “RE” in panels (b, c); in panel (c), the values are sum totals for these RE elements. Na, B, and Si, which are common glassware impurities, were excluded from ICP-MS analyses.

Table 3 | Summary of average A-site impurity concentrations (in weight-basis ppm) in metathesis/flux- and CVT-grown PdCoO₂ crystals, as determined by ICP-MS

A-site Elemental Impurities in PdCoO ₂				
	Ag (μg/g)	Hg (μg/g)	Cu (μg/g)	Pt (μg/g)
Flux	1.69 ± 0.01	BDL	0.50 ± 0.03	2.22 ± 0.02
CVT	0.78 ± 0.06	0.21 ± 0.02	0.4 ± 0.2	0.6 ± 0.2
DL	0.74	0.038	0.080	0.026

Shown are the concentrations of the only elements (four) that are known to adopt the A-site in ABO₂ delafossites and also fit the Pd site in PdCoO₂. The averages are over 2–3 runs on 1–3 crystals, and the uncertainties listed are standard deviations. Na, B, and Si, which are common glassware impurities, were excluded from all analyses. The detection limit (DL) is listed for each element; for concentrations below this detection limit, “BDL” is entered.

Table 4 | Summary of most prevalent B-site impurity average concentrations (in weight-basis ppm) in metathesis/flux- and CVT-grown PdCoO₂ crystals, as determined by ICP-MS

Most Prevalent B-site Elemental Impurities in PdCoO ₂							
	Al (μg/g)	Cr (μg/g)	Mn (μg/g)	Fe (μg/g)	Ni (μg/g)	Sn (μg/g)	Ir (μg/g)
Flux	82 ± 2	3.22 ± 0.09	13.3 ± 0.2	9.2 ± 0.2	15.0 ± 0.2	2.49 ± 0.04	1.08 ± 0.01
CVT	6.3 ± 0.8	3 ± 1	12 ± 6	9 ± 2	7 ± 3	1.61 ± 0.03	3 ± 1
DL	3.0	0.30	0.47	0.29	0.55	0.16	0.06

Shown are the concentrations of the seven most prevalent elements that fit the Co site in PdCoO₂. The averages are over 2–3 runs on 1–3 crystals, and the uncertainties listed are standard deviations. Na, B, and Si, which are common glassware impurities, were excluded from all analyses. The detection limit (DL) is listed for each element.

Discussion

The conclusion from the above is that the prototypical metallic delafossite PdCoO₂ is by no means ultrapure in general. Overall metals-basis impurity concentrations decrease from ~250 ppm in metathesis/flux crystals to ~50 ppm in CVT crystals but remain substantial. Crystal-chemical principles, however, dictate that the great majority of substitutional impurities must reside on the Co site, the relatively rare valence and coordination on the Pd site resulting in few elemental impurities (particularly Cu, Ag, and Pt) being capable of substitution. Sublattice purification ratios of ~1% thus arise, limiting the substitutional impurities on the Pd site to ~1 ppm. Our simple conclusion from these findings is that the electronic conduction in metallic delafossites such as PdCoO₂, which is strongly restricted to Pd *d* states at the Fermi level^{5,10,18–21}, thus occurs in highly pure Pd planes, with minimal substitutional impurities. This sublattice purification naturally explains how ultralow residual ρ_{ab} and extraordinary mean-free-paths can arise in metallic delafossite single crystals, despite the relatively dirty methods employed in their synthesis^{5,4}. Directly addressing a question posed in recent work⁵⁴, the BO₆ octahedral planes in metallic delafossites thus do host substantial disorder, in contrast to the Pd/Pt sheets, which were deduced to be highly perfect⁵⁴. The apparent contradiction of sizable magnetic impurity concentrations in crystals with high RRR is thus naturally resolved, as the majority of substitutional impurities, including magnetic ones, populate only the CoO₆ octahedra.

The above picture is predicated, however, on two key assumptions: that the ~1 ppm deduced impurity concentrations in the Pd planes are sufficiently low to facilitate the observed residual ρ_{ab} and mean-free-paths, and that the significant impurity concentrations in the BO₆ octahedral planes have sufficiently little impact on conduction in the Pd sheets. The first assumption can be addressed using the 2D unitary scattering approach recently applied by Sunko et al., which was validated in irradiated metallic delafossite crystals⁵⁴. This essentially assumes the strongest possible *s*-wave scattering⁵⁴ in a Drude model, resulting in $\rho = \frac{4\hbar n_d}{2e^2 n}$, where \hbar and e are the reduced Planck constant and electronic charge, n_d is the areal defect density, and n is the volume carrier density. Based on this, our deduced residual ρ_{ab} of 4 nΩcm would require a 2D defect density-of $6 \times 10^9 \text{ cm}^{-2}$ in CVT-grown PdCoO₂. This is in striking agreement with our determined Pd-sheet

impurity density, which corresponds to $5 \times 10^9 \text{ cm}^{-2}$ based on the 1.9 ppm of A-site impurities in Table 2. (This calculation takes into account the exact A-site impurity elements in Tables 2 and 3, and their relative masses). This indicates quantitative agreement between our deduced A-site impurity concentration and measured residual resistivity. This extends also to flux/metathesis crystals, where the A-site impurity concentration of 4.4 ppm in Table 2 would be expected to generate a residual ρ_{ab} of 7 nΩcm, very close to measured values¹⁷. (Again, this calculation takes into account the exact A-site impurity elements in Tables 2 and 3, and their relative masses; the distribution of impurities is different for CVT and metathesis/flux crystals). The second assumption is also supported by the recent work of Sunko et al., which explicitly concluded that disorder in the B-O layers must be efficiently screened;⁵⁴ the extent of this disorder was not determined in that paper, but is now known to be substantial (of order 100's of ppm).

Density functional theory (DFT) calculations provide further support for the above. These were performed (see “Methods” section) on PdCoO₂ lightly substituted with Pt, Ag, Fe, and Al, i.e., two known impurities on the Pd site and two prevalent impurities on the B site. $3 \times 3 \times 3$ supercells containing a single substituent atom were employed, i.e., 3.7% concentrations, as a computationally tractable approximation to the dilute limit. Unfolding of supercell bands was used to determine the effect of these impurities on the band structure and density-of-states (DOS) within the PdCoO₂ primitive cell. Figure 5 shows the resulting band structures in the left panels (a–d) and the corresponding DOS in the right panels (e–h). As might be expected, dilute Pt impurities on the A-site (Fig. 5a, e) have little effect on the band structure and DOS. The Pd *d* band crossing the Fermi energy (E_F) has no visible distortion at E_F in Fig. 5a, and the atom-projected DOS in Fig. 5e is of very similar form for Pd and Pt. Note here that the simulated Pd_{0.963}Pt_{0.037}CoO₂ has 26-times more Pd than Pt but no normalization is applied in Fig. 5e–h, simply to promote visibility of the impurity DOS. For Ag impurities (Fig. 5(b, f)), as might also be expected, the impacts on electronic structure are more significant. Some minor distortion of the Pd *d* band is visible, an impurity band forms ~100 meV below E_F , and there is some non-negligible weight crossing the Fermi level. Ag is thus a likely contributor to the unitary-limit scattering discussed above.

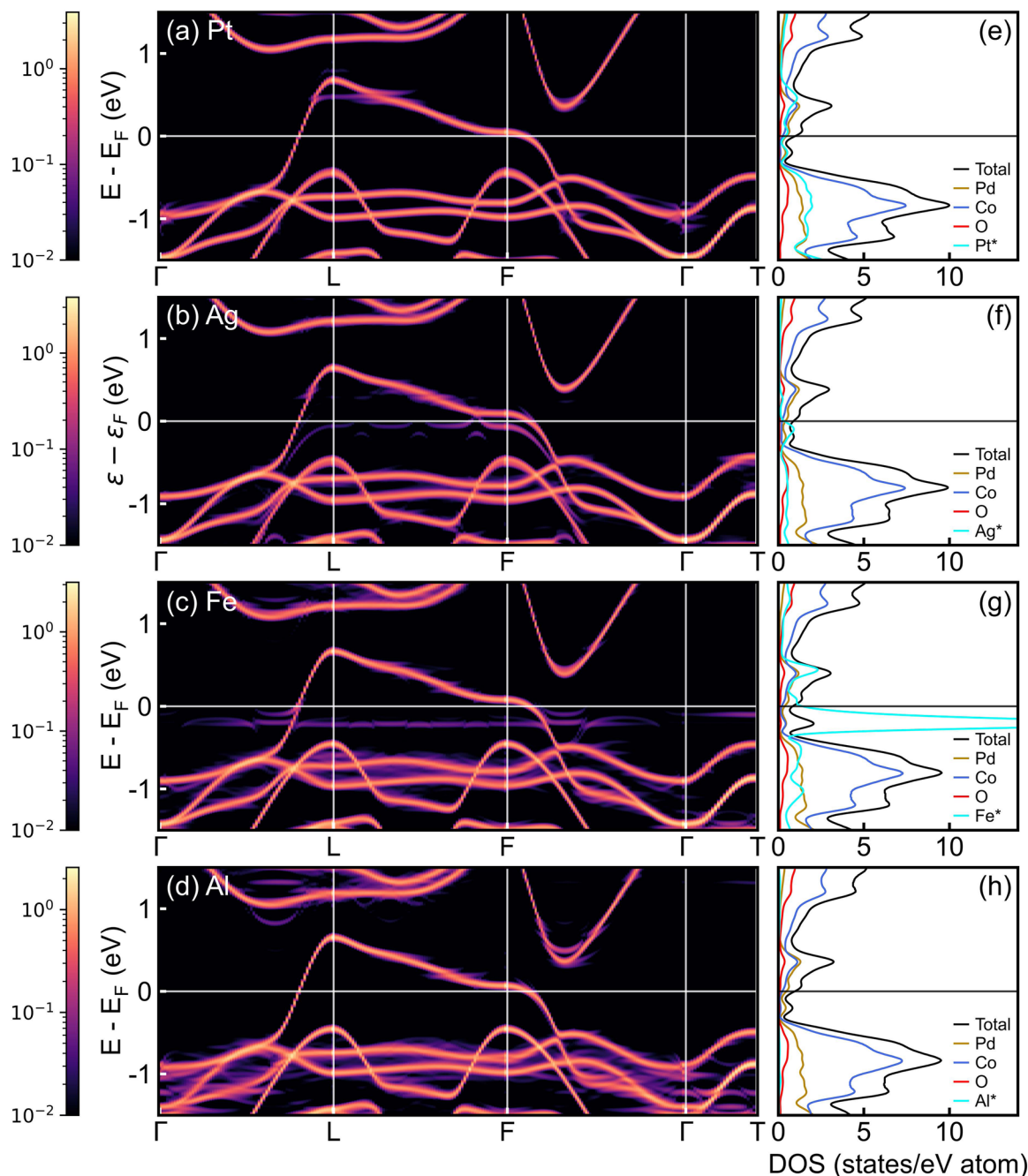


Fig. 5 | DFT-calculated electronic band structure and density-of-states of lightly-substituted PdCoO₂. **a–d** Band structure of Pd_{1-x}Pt_xCoO₂, Pd_{1-x}Ag_xCoO₂, PdCo_{1-x}Fe_xO₂, and PdCo_{1-x}Al_xO₂, respectively, for $x = 0.037$, i.e., 3.7% substitutional impurity density. Shown is the high-symmetry k -path Γ -L-F- Γ -T, in the first Brillouin zone, with energies relative to the Fermi energy, E_F . The intensities are on a \log_{10} scale depicting the weight of the unfolded primitive cell bands obtained from the supercell bands *via* the unfolding method^{77,78}. **e–h** Corresponding density-of-states

(DOS). Shown are the total DOS (black), and the atom-projected DOS of Pd (dark yellow), Co (blue), O (red), and the respective impurity (cyan). The DOS values are for the primitive cell, calculated by dividing by the corresponding number of atoms in the supercell. The atom-projected DOS curves for the impurity atoms (labeled with an asterisk) should thus be scaled by a factor of 0.037 for direct comparison; they are plotted here unscaled for improved visibility.

As might also be anticipated, the situation for Fe impurities on the B site is more complex. A narrow impurity band forms below E_F (Fig. 5c), generating a clear peak in the Fe-projected DOS in Fig. 5g, much larger than in Fig. 5f. Nevertheless, this main impurity band peak is centered at ~ 0.2 eV below E_F (many times $k_B T$ at the temperatures of interest in this work), and is quite narrow, meaning that the impact at E_F remains negligible even for Fe impurities. This directly supports the above conclusion that typical transition-metal B-site impurities (which are present at much lower concentrations in experiment) have only weak impact on conduction in the Pd planes of PdCoO₂. For Al

impurities (Fig. 5d, h), the absence of d electrons results in no significant effect on the band structure or DOS in the energy range in Fig. 5d, h, the only impact being some smearing of existing bands. This smearing is likely related to the larger structural distortions induced by Al impurities relative to Fe and Pt. The Pd-Pd length for Pd ions bonded via O in AlO₆ octahedra shifts by as much as 0.6%, for example, 1.5 times more than the equivalent for Fe impurities, and 5 times more than for Pt. Similarly, the average bond length in AlO₆ octahedra differ by $\sim 0.5\%$ from the CoO₆ octahedra in pristine PdCoO₂, much more than for the Fe case (0.02%). Figure 5 thus establishes that the B-site

impurities Fe and Al indeed have greater impact on the electronic structure than an A-site impurity such as Pt, but even Fe and Al have little meaningful impact in the vicinity of E_F , supporting our arguments.

It should be emphasized that the above analysis focuses on substitutional impurities. While interstitial impurities should also be considered, the delafossite structure is unlikely to host interstitial sites in which the ions in Fig. 4b can realistically be accommodated. The most obvious interstitial space involves an extra ion bonded to two O^{2-} ions in the adjacent B-O layer, for which DFT calculations suggest a formation energy as high as 6.3 eV in the case of Pd interstitials⁵⁴, consistent with the low interstitial volume. The equilibrium concentrations of such defects would thus be negligible, and would decrease for larger Ag, Pt, and Hg interstitials. With respect to vacancies, the above arguments strongly support that only Pd vacancies are of any real potential relevance for *a-b* plane metallic transport, as Co and O vacancies obviously reside in the insulating Co-O octahedral layers. The above quantitative agreement between measured residual resistivities and deduced Pd-layer substitutional impurity densities then strongly argues that any additional Pd vacancy effects are minor, in agreement with Sunko et al.⁵⁴. Beyond point defects, line and areal defects should be considered. As alluded to in the Introduction, however, current indications are that the densities of such defects are extraordinarily low in single-crystal metallic delafossites. This is supported by TEM observations^{54,60}, deductions from irradiation-induced defect studies⁵⁴, the substantial formation energies for most point defects in PdCoO₂⁵⁴, and the various additional observations of structural quality in the current paper, most notably the X-ray rocking curve widths (Fig. 2c inset). Substitutional impurities thus appear to be the key defects in metallic delafossites, which have been comprehensively elucidated here. Future work to more completely understand the reasons for the low density of line and areal defects in these compounds is nevertheless clearly important.

In summary, this work establishes CVT as a promising approach to bulk-single crystal growth of PdCoO₂, with potential applicability to other metallic delafossites such as PdCrO₂ and PdRhO₂. Compared to standard metathesis/flux methods, CVT generates orders-of-magnitude gains in crystal size and mass, along with the highest structural quality, highest purity, lowest magnetic impurity concentration, and highest RRR yet reported. Nevertheless, detailed trace impurity analysis of PdCoO₂ single crystals by ICP-MS reveals that, contrary to the naïve view, these metallic delafossites are not generally ultrapure; standard metathesis/flux methods result in ~250 ppm overall impurity concentrations, falling to ~50 ppm in CVT crystals. Simple crystal-chemistry-based analyses show that the vast majority of these impurities are forced to reside in the Co-O octahedral planes, however, only a small fraction being capable of substituting for Pd (typically a total of ~1 ppm of Cu, Ag, and Pt). The sublattice purification ratio is thus ~1%, resulting in ultrahigh purity in the Pd planes in which electronic conduction takes place, largely unaffected by the impurities in the CoO₆ octahedra. This sublattice purification mechanism is therefore central to the ultrahigh low-*T* conductivity of metallic delafossites, resolving the apparent contradiction that they appear impure from magnetometry yet highly pure in electronic transport. These results significantly demystify the outstanding low-*T* conductivity and mean-free-path in metallic delafossites, setting the stage for further advances with this extraordinary materials class. As an example, the analyses in Refs. 28,33 place PdCoO₂ in a situation where the momentum-conserving scattering rate is larger, but not much larger, than the momentum-relaxing scattering rate, leaving the system in a crossover regime between ballistic and viscous electronic transport. The momentum-conserving scattering is unlikely to be electron-electron scattering at the temperatures of interest³³ but could be electron-impurity scattering. It would thus be interesting to

understand whether the Co-O plane impurities elaborated here could be responsible for such. More broadly, the concepts developed in this work can also be expanded to other metallic and semiconducting delafossites, and potentially to other complex crystal families with very different valence/chemical environments for different cations.

Methods

Crystal growth

PdCoO₂ crystals were grown by two methods: the established metathesis/flux process⁶ and our CVT process¹⁸. The established process utilizes the metathesis reaction $PdCl_2 + Pd + Co_3O_4 \rightarrow 2PdCoO_2 + CoCl_2$ ⁶. Powders of PdCl₂ (ThermoFisher Scientific, 99.999% purity), Pd (Sigma-Aldrich, 99.995%), and Co₃O₄ (Alfa Aesar, 99.9985%) were mixed in a 1.5:1:1 molar ratio, then loaded and vacuum sealed (at 10⁻⁶ Torr) in quartz ampoules; excess PdCl₂ is reported to promote crystallization of PdCoO₂¹⁴. Ampoules were then heated to 700–750 °C at a ramp rate of 300 °C/h in a box furnace, dwelled for 40–150 h, cooled to 400 °C at 40–60 °C/h, then furnace cooled to ambient. These conditions were fine-tuned to optimize yield and phase purity. To remove excess PdCl₂ and the reaction by-product CoCl₂, the crystalline PdCoO₂ products (shown in Fig. 1b) were soaked in ethanol overnight then repeatedly washed in boiling ethanol until the effluent ran clear. Minor unreacted Pd and Co₃O₄ phases were often detected in these products by PXRD (see Supplementary Note 2). The largest crystals found in the products were 0.8 × 0.6 mm² laterally and 0.017 mm thick (Fig. 1b, inset).

For CVT, ~1 g of coarse-grained PdCoO₂ product from the above metathesis reaction was mixed with ~120 mg of PdCl₂ powder, then loaded and vacuum sealed (at 10⁻⁶ Torr) in quartz ampoules. Ampoules were then placed in a two-zone tube furnace with the reagents at one end of the ampoule (Fig. 1a). CVT was performed at a range of temperatures, spanning 740–800 °C for the hot zone and 680–750 °C for the cold-zone. Hot- and cold-zone temperatures of 760 and 710 °C were found optimal in terms of crystal size and complete transport (i.e., yield). For the first 3 days, the empty end of the tubes was maintained as the hot end, to clean the growth zone. The temperature gradient was then inverted for 13 days to establish the reagent-filled end of the tubes as the hot zone and the originally empty end as the cold/growth zone (Fig. 1a). We believe CVT to proceed via decomposition of PdCl₂ (above ~600 °C^{62,63}), followed by the reaction $PdCoO_2(s) + 2Cl_2(g) \leftrightarrow PdCl_2(g) + CoCl_2(g) + O_2(g)$ (Fig. 1a). Multicrystals up to 12 × 12 mm² laterally and 0.3 mm thick result from this process (Fig. 1c). Single crystals were then isolated by gently breaking the multicrystals apart, generating up to 6.0 × 4.0 mm² lateral sizes, with thickness up to 0.17 mm (see Fig. 1c, inset, for an example crystal). Excess chlorides were then removed by washing PdCoO₂ crystals in boiling ethanol. We are aware of no prior report of such CVT growth of metallic delafossites, although one approach to PdRhO₂ growth did employ a CVT-like temperature gradient⁵⁶ but with clear qualitative differences with our methods and findings.

Structural and chemical characterization

Optical microscope images of crystals were acquired with a Zeiss Axiovert A1 MAT inverted microscope, while SEM was performed in a JEOL JSM-6010PLUS/LA. EDS data were taken with an EDS detector integrated in the SEM, at 20 kV accelerating voltage. PIXE spectra were acquired in a MAS 1700 pelletron tandem ion accelerator (National Electrostatic Corp.) at 50 μC dose from a 4 MeV He²⁺ beam; PIXE data were analyzed using GUPIXWIN⁷⁰. Laue diffraction, PXRD, and single-crystal HRXRD (including rocking curves) were taken using Photonic Science back-reflection Laue, Rigaku MiniFlex 600, and Rigaku SmartLab XE diffractometer systems, respectively, the latter two with CuK_α radiation. PXRD analysis employed JADE for whole pattern fits, which were used to determine *a* and *c* lattice parameters. Laue analysis employed Lauesim⁷², modified for hexagonal symmetry.

Electronic transport and magnetometry measurements

Single crystals for electronic transport were first cleaved into bar shapes (Fig. 3a, inset) and affixed with GE varnish to Al₂O₃ wafers. Al contact wires were attached in a four-point in-line geometry to the top surface of the PdCoO₂ using ultrasonic wire bonding. *T*-dependent (~4–300 K) resistance measurements were then performed in a Janis cryostat/superconducting magnet, using a Lakeshore 370 AC resistance bridge and Lakeshore 3708 preamplifier/channel scanner (at 13.7 Hz and 10 mA). As alluded to in the main text and described in detail in Supplementary Note 3, great care was taken to accurately determine and account for instrumental voltage offsets, which are important due to the very low low-*T* resistance of PdCoO₂. A specialized protocol for this was developed and tested on zero-resistance superconducting V films. As also described in Supplementary Note 3, finite-element COMSOL simulations were performed to support the interpretation of the transport results, particularly with respect to the issue of systematic errors associated with the ρ_c/ρ_{ab} anisotropy. To minimize contamination for magnetometry measurements, crystals were first ground with thoroughly cleaned nonmagnetic tools then washed in ethanol to remove CoCl₂. The latter could occur not only at the original crystal surfaces but also at internal inclusions/voids¹⁶. Magnetometry was then done in a Quantum Design Physical Property Measurement System equipped with vibrating sample magnetometry (VSM) and high-*T* options, from 2 to 600 K in magnetic fields to 7 T.

Impurity analysis

For trace impurity analyses, ethanol-washed crystals were microwave digested in aqua regia (a 1:3 mixture of 70%-concentrated trace-metal-grade nitric acid (Ricca) and 36%-concentrated trace-metal-grade hydrochloric acid (Fisher Scientific)), or concentrated nitric acid, in sealed Teflon pressure vessels. A CEM MARS 5 microwave digestion system was employed, reaching 200 °C and ~15 bar for 2 h. Solutions were allowed to slow cool to room temperature overnight before serial dilution and analysis; no visible solid remained. Trace element analysis in a Thermo Scientific iCap TQ triple quadrupole ICP-MS system was performed by standard addition methods using SPEX CertiPrep and Thermo-Fisher Scientific multielement standards. Internal standard sets included: Sc, Y, Ir for alkali metals, alkaline-earth metals, non-precious transition metals, metalloids, and heavy metals; Sc, Y, Bi for precious metals; V, Rb, Cs, Bi for Sc, Y, and rare-earth elements. ICP-MS analytical details for each element are listed in Supplementary Table 6.

DFT calculations

First-principles density functional theory calculations were performed with the Quantum ESPRESSO package using norm-conserving pseudopotentials, with the exchange-correlation energy approximated by the Perdew-Burke-Ernzerhof functional^{73–75}. The energy cutoff for the plane waves was set to 100 Ry. Dilute impurities on the Pd- and Co-sites (i.e., Pd_{1-x}Z_xCoO₂ and PdCo_{1-x}Z_xO₂) were simulated in a 3 × 3 × 3 supercell with 108 atoms, with one Pd or Co atom replaced, corresponding to *x* = 0.037. Pt and Ag substituted for Pd, and Fe and Al substituted for Co were considered. Both the unit cell shape and atomic positions were relaxed for electronic structure calculations. The band structure and DOS were calculated on a Γ -centered Monkhorst-Pack grid of 4 × 4 × 4 *k* points in the Brillouin zone of the supercell. The unfolded band structures in Fig. 5 were obtained using the bandUPpy code^{76–78}. The unfolding method projects a wave vector **K** in the supercell Brillouin zone onto a corresponding wave vector **k** in the primitive cell Brillouin zone via a supercell reciprocal lattice vector. This unfolding evaluates the spectral weight or probability of finding a set of primitive-cell Bloch states at wave vector **k** that are contributing to the supercell eigenstates at wave vector **K** at the same energy. The specific

method adopted here⁷⁷ finds the effective band structure for doped PdCoO₂ by using the spectral function to calculate the weight, which is given by the number of primitive cell bands that are crossing within a small energy window around the band center.

Data availability

All data needed to evaluate the conclusions presented in this study have been deposited in DRUM (Data Repository for the University of Minnesota) at: <https://doi.org/10.13020/Ok3v-jj67>. Any additional digital data are available from the corresponding author upon request.

References

- Imada, M., Fujimori, A. & Tokura, Y. Metal-insulator transitions. *Rev. Mod. Phys.* **70**, 1039–1263 (1998).
- Hwang, H. Y. et al. Emergent phenomena at oxide interfaces. *Nat. Mater.* **11**, 103–113 (2012).
- Ramesh, R. & Schlom, D. G. Whither oxide electronics? *MRS Bull.* **33**, 1006–1014 (2008).
- Mannhart, J. & Schlom, D. G. Oxide interfaces—an opportunity for electronics. *Science* **327**, 1607–1611 (2010).
- Mackenzie, A. P. The properties of ultrapure delafossite metals. *Rep. Prog. Phys.* **80**, 032501 (2017).
- Shannon, R. D., Rogers, D. B. & Prewitt, C. T. Chemistry of noble metal oxides. I. Syntheses and properties of ABO₂ delafossite compounds. *Inorg. Chem.* **10**, 713–718 (1971).
- Prewitt, C. T., Shannon, R. D. & Rogers, D. B. Chemistry of noble metal oxides. II. Crystal structures of platinum cobalt dioxide, palladium cobalt dioxide, copper iron dioxide, and silver iron dioxide. *Inorg. Chem.* **10**, 719–723 (1971).
- Rogers, D. B., Shannon, R. D., Prewitt, C. T. & Gillson, J. L. Chemistry of noble metal oxides. III. Electrical transport properties and crystal chemistry of ABO₂ compounds with the delafossite structure. *Inorg. Chem.* **10**, 723–727 (1971).
- Daou, R., Frésard, R., Eyert, V., Hébert, S. & Maignan, A. Unconventional aspects of electronic transport in delafossite oxides. *Sci. Technol. Adv. Mater.* **18**, 919–938 (2017).
- Lechermann, F. From basic properties to the Mott design of correlated delafossites. *npj Comput. Mater.* **7**, 120 (2021).
- Mekata, M., Yaguchi, N., Takagi, T., Mitsuda, S. & Yoshizawa, H. Magnetic ordering in delafossite CuFeO₂. *J. Magn. Magn. Mater.* **104–107**, 823–824 (1992).
- Ye, F. et al. Magnetic interactions in the geometrically frustrated triangular lattice antiferromagnet CuFeO₂. *Phys. Rev. Lett.* **99**, 157201 (2007).
- Kawazoe, H. et al. P-type electrical conduction in transparent thin films of CuAlO₂. *Nature* **389**, 939–942 (1997).
- Takatsu, H. et al. Roles of high-frequency optical phonons in the physical properties of the conductive delafossite PdCoO₂. *J. Phys. Soc. Jpn.* **76**, 104701 (2007).
- Hicks, C. W. et al. Quantum oscillations and high carrier mobility in the delafossite PdCoO₂. *Phys. Rev. Lett.* **109**, 116401 (2012).
- Tanaka, M., Hasegawa, M. & Takei, H. Growth and anisotropic physical properties of PdCoO₂ single crystals. *J. Phys. Soc. Jpn.* **65**, 3973–3977 (1996).
- Nandi, N. et al. Unconventional magneto-transport in ultrapure PdCoO₂ and PtCoO₂. *npj Quantum Mater.* **3**, 66 (2018).
- Zhang, Y. et al. Thermal properties of the metallic delafossite PdCoO₂: a combined experimental and first-principles study. *Phys. Rev. Mater.* **6**, 115004 (2022).
- Ong, K. P., Zhang, J., Tse, J. S. & Wu, P. Origin of anisotropy and metallic behavior in delafossite PdCoO₂. *Phys. Rev. B* **81**, 115120 (2010).
- Eyert, V., Frésard, R. & Maignan, A. On the metallic conductivity of the delafossites PdCoO₂ and PtCoO₂. *Chem. Mater.* **20**, 2370–2373 (2008).

21. Kim, K., Choi, H. C. & Min, B. I. Fermi surface and surface electronic structure of delafossite PdCoO₂. *Phys. Rev. B* **80**, 35116 (2009).
22. Seshadri, R., Felser, C., Thieme, K. & Tremel, W. Metal–metal bonding and metallic behavior in some ABO₂ delafossites. *Chem. Mater.* **10**, 2189–2196 (1998).
23. Tanaka, M. et al. Origin of the metallic conductivity in PdCoO₂ with delafossite structure. *Phys. B Condens. Matter* **245**, 157–163 (1998).
24. Yao, X., Xun, Y., Zhu, Z., Zhao, S. & Li, W. Origin of the high electrical conductivity of the delafossite metal PdCoO₂. *Phys. Rev. B* **109**, 075110 (2024).
25. Noh, H.-J. et al. Anisotropic electric conductivity of delafossite PdCoO₂ studied by angle-resolved photoemission spectroscopy. *Phys. Rev. Lett.* **102**, 256404 (2009).
26. Mazzola, F. et al. Itinerant ferromagnetism of the Pd-terminated polar surface of PdCoO₂. *Proc. Natl Acad. Sci. USA* **115**, 12956–12960 (2018).
27. Sunko, V. *Angle Resolved Photoemission Spectroscopy of Delafossite Metals* (Max Planck Institute for Chemical Physics of Solids, 2019).
28. Moll, P. J. W., Kushwaha, P., Nandi, N., Schmidt, B. & Mackenzie, A. P. Evidence for hydrodynamic electron flow in PdCoO₂. *Science* **351**, 1061–1064 (2016).
29. Putzke, C. et al. h/e oscillations in interlayer transport of delafossites. *Science* **368**, 1234–1238 (2020).
30. Takatsu, H. et al. Extremely large magnetoresistance in the non-magnetic metal PdCoO₂. *Phys. Rev. Lett.* **111**, 56601 (2013).
31. Harada, T. et al. Anomalous Hall effect at the spontaneously electron-doped polar surface of PdCoO₂ ultrathin films. *Phys. Rev. Res.* **2**, 13282 (2020).
32. Mazzola, F. et al. Tuneable electron–magnon coupling of ferromagnetic surface states in PdCoO₂. *npj Quantum Mater.* **7**, 20 (2022).
33. Baker, G. et al. Non-local electrodynamics in ultra-pure PdCoO₂. *Phys. Rev. X* <https://journals.aps.org/prx/accepted/6a078K22Fe61940cf6db5bf5e0050665ea387d3da> (2023).
34. Bachmann, M. D. et al. Directional ballistic transport in the two-dimensional metal PdCoO₂. *Nat. Phys.* **18**, 819–824 (2022).
35. Bachmann, M. D. et al. Super-geometric electron focusing on the hexagonal Fermi surface of PdCoO₂. *Nat. Commun.* **10**, 5081 (2019).
36. McGuinness, P. H. et al. Low-symmetry nonlocal transport in microstructured squares of delafossite metals. *Proc. Natl Acad. Sci. USA* **118**, e2113185118 (2021).
37. Doumerc, J.-P., Wichainchai, A., Ammar, A., Pouchard, M. & Hagenmuller, P. On magnetic properties of some oxides with delafossite-type structure. *Mater. Res. Bull.* **21**, 745–752 (1986).
38. Mekata, M., Sugino, T., Oohara, A., Oohara, Y. & Yoshizawa, H. Magnetic structure of antiferromagnetic PdCrO₂ possible degenerate helices on a rhombohedral lattice. *Phys. B Condens. Matter* **213–214**, 221–223 (1995).
39. Takatsu, H., Yoshizawa, H., Yonezawa, S. & Maeno, Y. Critical behavior of the metallic triangular-lattice Heisenberg antiferromagnet PdCrO₂. *Phys. Rev. B* **79**, 104424 (2009).
40. Takatsu, H. et al. Magnetic structure of the conductive triangular-lattice antiferromagnet PdCrO₂. *Phys. Rev. B* **89**, 104408 (2014).
41. Takatsu, H., Yonezawa, S., Fujimoto, S. & Maeno, Y. Unconventional anomalous hall effect in the metallic triangular-lattice magnet PdCrO₂. *Phys. Rev. Lett.* **105**, 137201 (2010).
42. Ok, J. M. et al. Quantum oscillations of the metallic triangular-lattice antiferromagnet PdCrO₂. *Phys. Rev. Lett.* **111**, 176405 (2013).
43. Zhakina, E. et al. Investigation of Planckian behavior in a high-conductivity oxide: PdCrO₂. *Proc. Natl Acad. Sci.* **120**, e2307334120 (2023).
44. Mendez-Valderrama, J. F. et al. T-linear resistivity from magneto-elastic scattering: application to PdCrO₂. *Proc. Natl Acad. Sci.* **120**, e2305609120 (2023).
45. Kumar, S., Multunas, C., Defay, B., Gall, D. & Sundaraman, R. Ultralow electron-surface scattering in nanoscale metals leveraging Fermi-surface anisotropy. *Phys. Rev. Mater.* **6**, 85002 (2022).
46. Harada, T. Thin-film growth and application prospects of metallic delafossites. *Mater. Today Adv.* **11**, 100146 (2021).
47. Harada, T. & Okada, Y. Metallic delafossite thin films for unique device applications. *APL Mater.* **10**, 70902 (2022).
48. Harada, T., Ito, S. & Tsukazaki, A. Electric dipole effect in PdCoO₂/β-Ga₂O₃ Schottky diodes for high-temperature operation. *Sci. Adv.* **5**, eaax5733 (2019).
49. Li, G. et al. In situ modification of a delafossite-type PdCoO₂ bulk single crystal for reversible hydrogen sorption and fast hydrogen evolution. *ACS Energy Lett.* **4**, 2185–2191 (2019).
50. Harada, T., Fujiwara, K. & Tsukazaki, A. Highly conductive PdCoO₂ ultrathin films for transparent electrodes. *APL Mater.* **6**, 046107 (2018).
51. Yordanov, P. et al. Generation of terahertz radiation via the transverse thermoelectric effect. *Adv. Mater.* **35**, 2305622 (2023).
52. Klobes, B. et al. Anisotropic lattice dynamics and intermediate-phase magnetism in delafossite CuFeO₂. *Phys. Rev. B* **92**, 14304 (2015).
53. Bansal, D. et al. Lattice dynamics and thermal transport in multiferroic CuCrO₂. *Phys. Rev. B* **95**, 54306 (2017).
54. Sunko, V. et al. Controlled introduction of defects to delafossite metals by electron irradiation. *Phys. Rev. X* **10**, 21018 (2020).
55. Daou, R., Frésard, R., Hébert, S. & Maignan, A. Large anisotropic thermal conductivity of the intrinsically two-dimensional metallic oxide PdCoO₂. *Phys. Rev. B* **91**, 41113 (2015).
56. Kushwaha, P. et al. Single crystal growth, structure, and electronic properties of metallic delafossite PdRhO₂. *Cryst. Growth Des.* **17**, 4144–4150 (2017).
57. Kushwaha, P. et al. Nearly free electrons in a 5d delafossite oxide metal. *Sci. Adv.* **1**, e1500692 (2015).
58. Tanaka, M., Hasegawa, M. & Takei, H. Crystal growth of PdCoO₂, PtCoO₂ and their solid-solution with delafossite structure. *J. Cryst. Growth* **173**, 440–445 (1997).
59. Takatsu, H. & Maeno, Y. Single crystal growth of the metallic triangular-lattice antiferromagnet PdCrO₂. *J. Cryst. Growth* **312**, 3461–3465 (2010).
60. Chang, C. S. et al. Visualization of defects in single-crystal and thin-film PdCoO₂ using aberration-corrected scanning transmission electron microscopy. *Phys. Rev. Mater.* **6**, 93401 (2022).
61. Usui, H. et al. Hidden kagome-lattice picture and origin of high conductivity in delafossite PtCoO₂. *Phys. Rev. Mater.* **3**, 45002 (2019).
62. Renner, H. et al. Platinum group metals and compounds. In *Ullmann's Encyclopedia of Industrial Chemistry* 1–73 (Wiley, 2018).
63. Oranskaya, M. A. & Mikhailova, N. A. Dissociation pressure and vapour pressure of palladium chloride. *Russ. J. Inorg. Chem.* **5**, 5–7 (1960).
64. Voigt, B. et al. Transport evidence for sulfur vacancies as the origin of unintentional n-Type doping in pyrite FeS₂. *ACS Appl. Mater. Interfaces* **11**, 15552–15563 (2019).
65. Brooks, C. M. et al. Growth of homoepitaxial SrTiO₃ thin films by molecular-beam epitaxy. *Appl. Phys. Lett.* **94**, 162905 (2009).
66. Ambwani, P. et al. Defects, stoichiometry, and electronic transport in SrTiO_{3-δ} epilayers: a high pressure oxygen sputter deposition study. *J. Appl. Phys.* **120**, 55704 (2016).
67. Breckenfeld, E. et al. Effect of growth induced (non)stoichiometry on the structure, dielectric response, and thermal conductivity of SrTiO₃ thin films. *Chem. Mater.* **24**, 331–337 (2012).

68. Ohnishi, T., Shibuya, K., Yamamoto, T. & Lippmaa, M. Defects and transport in complex oxide thin films. *J. Appl. Phys.* **103**, 103703 (2008).
69. Jalan, B., Moetakef, P. & Stemmer, S. Molecular beam epitaxy of SrTiO₃ with a growth window. *Appl. Phys. Lett.* **95**, 32906 (2009).
70. GUPIXWIN 2.1.4. computer program at <https://www.physics.uoguelph.ca/about-gupix-and-gupixwin> (2005).
71. Hasegawa, M., Tanaka, M. & Takei, H. Metathetical reaction growth and characterization of delafossite-type Pd(Co,Mg)O₂ single crystals. *J. Cryst. Growth* **226**, 277–280 (2001).
72. Pang, E. lauesim. computer program at <https://github.com/epang22/lauesim> (2019).
73. Giannozzi, P. et al. QUANTUM ESPRESSO: a modular and open-source software project for quantum simulations of materials. *J. Phys. Condens. Matter* **21**, 395502 (2009).
74. Perdew, J. P., Burke, K. & Ernzerhof, M. Generalized gradient approximation made simple. *Phys. Rev. Lett.* **77**, 3865–3868 (1996).
75. van Setten, M. J. et al. The PseudoDojo: Training and grading a 85 element optimized norm-conserving pseudopotential table. *Comput. Phys. Commun.* **226**, 39–54 (2018).
76. Tsirkin, S., Novianus, A. & Cheng, N. bandUPpy. computer program at <https://github.com/band-unfolding/banduppy> (2023).
77. Medeiros, P. V. C., Stafström, S. & Björk, J. Effects of extrinsic and intrinsic perturbations on the electronic structure of graphene: retaining an effective primitive cell band structure by band unfolding. *Phys. Rev. B* **89**, 41407 (2014).
78. Medeiros, P. V. C., Tsirkin, S. S., Stafström, S. & Björk, J. Unfolding spinor wave functions and expectation values of general operators: introducing the unfolding-density operator. *Phys. Rev. B* **91**, 41116 (2015).
79. Villars, P. & Cenzual, K. PdCoO₂ Crystal Structure: sd_1920856 data sets. in *PAULING FILE in Inorganic Solid Phases*. https://materials.springer.com/isp/crystallographic/docs/sd_1920856 (2016).
80. Shannon, R. D. & Prewitt, C. T. Effective ionic radii in oxides and fluorides. *Acta Crystallogr.* **B25**, 925–946 (1969).
81. Wagner, F. E. et al. Before striking gold in gold-ruby glass. *Nature* **407**, 691–692 (2000).

Acknowledgements

We thank Prof. Xinyuan Zhang for useful advice on ICP-MS analysis. This work was primarily supported by the US Department of Energy through the University of Minnesota (UMN) Center for Quantum Materials, under Grant No. DE-SC0016371 (CL). Parts of this work were carried out in the Characterization Facility, UMN, which receives partial support from the National Science Foundation through the MRSEC (Award Number DMR-2011401) and NNCI (Award Number ECCS-2025124) programs. The Minnesota Supercomputing Institute at UMN provided resources that contributed to the research reported within this paper.

Author contributions

CL conceived the study and supervised its execution. YZ and FT grew the crystals, which were structurally and chemically characterized by YZ, FT, GH, MM, and JG-B. YZ, FT, BK, JR, and VC performed the transport and magnetometry measurements. YZ, SB, and YT performed Laue characterization and analysis. YZ, GE, and WS performed mass spectrometry measurements and analysis. PS, TB, and RF performed the theoretical work. CL and YZ wrote the paper, with input from all authors.

Competing interests

The authors declare no competing interests.

Additional information

Supplementary information The online version contains supplementary material available at <https://doi.org/10.1038/s41467-024-45239-6>.

Correspondence and requests for materials should be addressed to Chris Leighton.

Peer review information *Nature Communications* thanks Douglas Bonn, Andrew Mackenzie and the other, anonymous, reviewer(s) for their contribution to the peer review of this work. A peer review file is available.

Reprints and permissions information is available at <http://www.nature.com/reprints>

Publisher's note Springer Nature remains neutral with regard to jurisdictional claims in published maps and institutional affiliations.

Open Access This article is licensed under a Creative Commons Attribution 4.0 International License, which permits use, sharing, adaptation, distribution and reproduction in any medium or format, as long as you give appropriate credit to the original author(s) and the source, provide a link to the Creative Commons license, and indicate if changes were made. The images or other third party material in this article are included in the article's Creative Commons license, unless indicated otherwise in a credit line to the material. If material is not included in the article's Creative Commons license and your intended use is not permitted by statutory regulation or exceeds the permitted use, you will need to obtain permission directly from the copyright holder. To view a copy of this license, visit <http://creativecommons.org/licenses/by/4.0/>.

© The Author(s) 2024